A&A 472, 623–632 (2007)
DOI: 10.1051/0004-6361:20066961

Astronomy & Astrophysics

Particle acceleration by fluctuating electric fields at a magnetic field null point

P. Petkaki[1] and A. L. MacKinnon[2]

[1] Physical Sciences Division, British Antarctic Survey, Cambridge CB3 0ET, UK
e-mail: ppe@bas.ac.uk
[2] DACE/Physics and Astronomy, University of Glasgow, Glasgow G12 8QQ, UK

Received 18 December 2006 / Accepted 22 June 2007

ABSTRACT

Context. Particle acceleration consequences from fluctuating electric fields superposed on an X-type magnetic field in collisionless solar plasma are studied. Such a system is chosen to mimic generic features of dynamic reconnection, or the reconnective dissipation of a linear disturbance.
Aims. We explore numerically the consequences for charged particle distributions of fluctuating electric fields superposed on an X-type magnetic field.
Methods. Particle distributions are obtained by numerically integrating individual charged particle orbits when a time varying electric field is superimposed on a static X-type neutral point. This configuration represents the effects of the passage of a generic MHD disturbance through such a system. Different frequencies of the electric field are used, representing different possible types of wave. The electric field reduces with increasing distance from the X-type neutral point as in linear dynamic magnetic reconnection.
Results. The resulting particle distributions have properties that depend on the amplitude and frequency of the electric field. In many cases a bimodal form is found. Depending on the timescale for variation of the electric field, electrons and ions may be accelerated to different degrees and often have energy distributions of different forms. Protons are accelerated to γ-ray producing energies and electrons to and above hard X-ray producing energies in timescales of 1 s. The acceleration mechanism is possibly important for solar flares and solar noise storms but is also applicable to all collisionless plasmas.

Key words. acceleration of particles – waves – Sun: flares – Sun: X-rays – gamma rays

1. Introduction

Release of stored magnetic energy via particle acceleration is a characteristic feature of astrophysical plasmas. In the particular case of the Sun, we see this manifested in the catastrophic events of flares, as well as in quieter phenomena like radio noise storms. Similar phenomena are observed in other late-type stars, and similar physics may be involved in understanding a wide variety of astrophysical objects (see e.g. Kuijpers 1993; Hanasz & Lesch 2003).

The special case of solar flares involves particular challenges to theory. A large fraction (several tens of percent) of the flare energy is manifested initially in the form of fast electrons (accelerated out of the background distribution to ~100 keV in about 1 s and to ~100 MeV in a few seconds), which reveal their presence by producing bremsstrahlung X-rays (e.g. Miller 1998; MacKinnon 2006). Protons are accelerated in flares to energies of several tens of MeVs in a timescale of one second (Miller 1998; Aschwanden 2002). Thus the acceleration of particles is an important part of the energy release process, rather than an energetically unimportant consequence of the flare. Moreover, radio signatures (type I noise storms, type III bursts away from flares) testify to particle acceleration at "quiet" times.

Magnetic reconnection is one of the primary candidate mechanisms for releasing non-potential energy from magnetized plasmas (e.g. Priest & Forbes 2001). The electric field in the current-carrying region also makes it a natural particle accelerator. Collision-dominated sheets will involve the production of some runaway particles, but almost by definition particle acceleration is not a primary consequence of such a situation (e.g. Smith 1980). However, Martens (1988) gave order-of-magnitude arguments in favor of a collisionless current sheet as both the energy release mechanism and the particle accelerator in flares. Particle acceleration is energetically the primary consequence of such a situation. Collisionless reconnection thus assumes great potential importance in understanding the flare process, particle acceleration, energy conversion and release in astrophysical plasmas generally (Petkaki & MacKinnon 1997; Heerikhuisen et al. 2002; Hamilton et al. 2003; Turkmani et al. 2006; Wood & Neukirch 2005; Vainchtein et al. 2005; McClements et al. 2006).

Here we present test particle calculations designed to illuminate the consequences for particle acceleration of dynamic reconnection. We have in mind particularly the picture of Craig & McClymont (1991, 1993), in which a linear disturbance passes through a magnetic configuration containing an X-type neutral point. The disturbance travels non-dissipatively with the local Alfvén speed until it approaches the dissipation region surrounding the neutral point, where the resistive diffusion term in the induction equation becomes important. The wave damps resistively in a few system transit times, with consequences (heating or particle acceleration) determined by the physical nature of the resistivity. Several assumptions were made in Craig and McClymont's original discussion (linear disturbance, cold plasma limit, 2D, Ohm's law including only a scalar resistivity) but this essential picture still affords a qualitative guide in more

complex situations (e.g. McClymont & Craig 1996; Senanayake & Craig 2006).

In Petkaki & MacKinnon (1997), we examined the behavior of protons in the presence of electric and magnetic fields obtained from the Craig & McClymont (1991) analysis. Here we carry out a complementary exercise, studying test particle evolution in the presence of simple fields chosen to mimic generic features of dynamic reconnection. Our aim is to comment on particle acceleration consequences, in a parametric way that does not depend on a particular set of simplifying physical assumptions or boundary conditions. Time-dependence of the electric field is the essential ingredient reflecting the dynamic character of the reconnection. We present examples of distributions resulting from a time-independent electric field for comparison and highlight distinct features of the distributions resulting from dynamic situations.

We use the Craig & McClymont (1991) linear solution as a qualitative guide for the spatial and temporal form of the electric field. Our adopted field also resembles a linear situation in displaying a time dependence that does not change (i.e. does not develop multiple frequencies, saturate, etc.). Basing our calculations on this linear picture makes it unlikely that they will provide a complete description of what happens in a flare, although they offer useful insight. They may however be particularly relevant to non-flaring particle acceleration, e.g. in solar noise storms, or as part of the explanation of "quiescent" radio emission seen from RS CVn binaries (Kuijpers & van der Hulst 1985).

Since we aim to emulate a linear situation we may pick our test particles from an isotropic, homogeneous distribution representing the background. This is in contrast to particle studies of nonlinear reconnection, where consistency demands consideration of the motion of particles into the dissipation region. In most studies particles are injected in two opposite quadrupoles of the X-point and they subsequently are driven, by the $\underline{E} \times \underline{B}$ drift due to an imposed constant electric field, to cross the nonadiabatic region or miss it depending on their initial conditions (see e.g. Burkhart et al. 1990).

Many previous studies of test particle evolution in steady reconnection exist. Here we mention particularly the work of Martin (1986), which demonstrates that the orbits of such test particles are chaotic, and of Burkhart et al. (1990, 1991) who iterated from the test particle calculations to construct a self-consistent description of the diffusion region. Recent work studies regular and chaotic dynamics in 3D reconnecting current sheets (Efthymiopoulos et al. 2005; Gontikakis et al. 2006) or studies particle orbits in the presence of 3D magnetic nulls (Heerikhuisen et al. 2002; Dalla & Browning 2005). Particularly relevant here is the exploratory, analytical study of Litvinenko (2003) which looks at charged particle orbits in an oscillating electric field in a magnetic field containing a neutral line.

The next section gives details of the specific model we adopt in order to study particle acceleration in time-dependent reconnection, while Sect. 3 describes our results for particle distributions. Section 4 discusses some possible implications of our results.

2. Model for particle acceleration in fluctuating electric fields

We are going to study the evolution of test particles in the presence of electromagnetic fields chosen to mimic generic features of dynamic reconnection. Time-dependence of the electric field reflects the dynamic character of the reconnection.

2.1. Equations of motion

We solve numerically the relativistic equations of motions of test particles (particles are expected to acquire relativistic velocities) in electromagnetic fields and in the observer's reference frame:

$$\frac{\mathrm{d}\underline{r}}{\mathrm{d}t} = \frac{\underline{p}}{m\gamma} \tag{1}$$

$$\frac{\mathrm{d}\underline{p}}{\mathrm{d}t} = q\left(\underline{E} + \frac{1}{c}(\underline{u} \times \underline{B})\right) \tag{2}$$

where $\gamma = (1 - (u/c)^2)^{-1/2}$, $\underline{u} = \underline{p}/m\gamma$.

To model the reconnection magnetic field, we adopt an idealized 2D magnetic field containing an X-type neutral point:

$$\underline{B} = \frac{B_0}{D}(y\hat{x} + x\hat{y}). \tag{3}$$

The current density vanishes for this field configuration. The field lines are the solutions of $\frac{\mathrm{d}x}{\mathrm{d}y} = \frac{y}{x}$ which are hyperbolae $y^2 - x^2 = \text{const}$. The X-line (neutral line) lies along the z-axis. The field strength depends on position thus:

$$|\underline{B}| = B_0 \frac{r}{D} \tag{4}$$

where $x^2 + y^2 = r^2$. Note that this configuration has no natural scale length. Requiring the field to have a value of 10^2 Gauss at a typical active region distance of 10^9 cm from the neutral point, fixes only $B_0/D = 10^{-7}$ Gauss cm^{-1}. We are free to use other considerations to fix one of B_0 and D independently, as we do below in introducing dimensionless variables. An electric field is imposed in the z direction, with spatial and temporal form chosen to mimic qualitative features of dynamic reconnection (see Sect. 2.2).

We normalize distances to D_n and times to the gyroperiod at $r = D_n$. We denote the resulting timescales by τ_p and τ_e for the cases of electrons and protons respectively. As noted above, D_n is as yet undetermined. It turns out to be convenient in this relativistic calculation to choose D_n such that velocities are normalized to the speed of light. This has the consequence that D_n takes different values $D_\mathrm{e} = c\sqrt{(m_\mathrm{e} D/eB_0)}$ and $D_\mathrm{p} = c\sqrt{(m_\mathrm{p} D/eB_0)}$ for electrons and protons respectively (Petkaki & MacKinnon 1994; Petkaki 1996), such that

$$D_\mathrm{p} = \left(\frac{m_\mathrm{p}}{m_\mathrm{e}}\right)^{\frac{1}{2}} D_\mathrm{e}. \tag{5}$$

Specifically, with $B_0/D = 10^{-7}$, we find $D_\mathrm{e} = 1.3 \times 10^5$ cm and $D_\mathrm{p} = 5.6 \times 10^6$ cm. With our choices of $\underline{E}$ and $\underline{B}$ the Lorentz Eqs. (1) and (2) become in three dimensions and in dimensionless units:

$$\begin{aligned}
\frac{\mathrm{d}\bar{x}}{\mathrm{d}\bar{t}} &= \bar{u}_x = \frac{\bar{p}_x}{\gamma} \\
\frac{\mathrm{d}\bar{y}}{\mathrm{d}\bar{t}} &= \bar{u}_y = \frac{\bar{p}_y}{\gamma} \\
\frac{\mathrm{d}\bar{z}}{\mathrm{d}\bar{t}} &= \bar{u}_z = \frac{\bar{p}_z}{\gamma} \\
\frac{\mathrm{d}\bar{p}_x}{\mathrm{d}\bar{t}} &= -\epsilon \bar{x} \bar{u}_z \\
\frac{\mathrm{d}\bar{p}_y}{\mathrm{d}\bar{t}} &= \epsilon \bar{y} \bar{u}_z \\
\frac{\mathrm{d}\bar{p}_z}{\mathrm{d}\bar{t}} &= \bar{E} + \epsilon(\bar{x}\bar{u}_x + \bar{y}\bar{u}_y)
\end{aligned} \tag{6}$$

where $\gamma = (1 + {p_x}^2 + {p_y}^2 + {p_z}^2)^{\frac{1}{2}}$ and $\epsilon = +1$ for protons, $\epsilon = -1$ for electrons. $E(\underline{r}, t)$ is the true value of the electric field and $\bar{E} = E(D/B_0)D_i$ is the dimensionless electric field, with subscript i taking the values e for electrons or p for protons. Energies are now normalised to the particle rest mass energy so that kinetic energy in dimensionless units is just $K_{\rm kin} = \gamma - 1$. Equations (6) with appropriate initial conditions and a specific form for $\bar{E}$ describe the motion of a particle.

2.2. Electric field

Craig & McClymont (1991) guide us in adopting a functional form of electric field which allows us to investigate consequences of time-dependence in a parametric way. Their resistively damping, linear disturbance involves a regularly oscillating electric field whose amplitude is greatest in the region near the neutral point where the resistive term of the induction equation becomes important. Far from this region the disturbance is Alfvénic in character and dominated by the boundary conditions, so that the electric field amplitude always maximises in the central, diffusion region (see also Petkaki & MacKinnon 1997, Sect. 3). Thus we adopt the following form for the electric field $\underline{E}$:

$$\underline{E} = E_0 \sin(\omega t)\hat{z} f(x, y) \tag{7}$$

where $f(x, y)$ describes the spatial variation of $\underline{E}$. We take

$$f(x, y) = \exp(-\alpha_i \sqrt{(|r|)}) \tag{8}$$

where, $\alpha_{\rm p} = 2.5 \times 10^{-1}$, $\alpha_{\rm e} = 3.776 \times 10^{-2}$, $|r| = \sqrt{(x^2 + y^2)}$. Consistent with our concentration on particle acceleration near the neutral point and with in situ measurements in Earth's magnetosphere (Øieroset et al. 2001), we expect that resistivity will be primarily inertial in character (Speiser 1970). As shown in Fig. 1, this form approximates the radial form of the electric field calculated from the Craig & McClymont (1991) solution, for an (inertial) resistivity η estimated assuming the dominant contribution from 1 keV protons (see Petkaki & MacKinnon 1997, Sect. 3; Speiser 1970). The form of the electric field is shown in Fig. 1 at $t = 0$. The exact Craig and McClymont solution develops more complex spatial structure but the spatial form of Eq. (8) thus embodies a dissipation region on the appropriate length scale.

The frequency of oscillation of the electric field which we denote by ω is a free parameter. Each simulation uses one value of ω. We take values of ω such that $1/1000 < \omega < 10\,000$, corresponding to a broadband wave spectrum which may propagate in such a system (see Petkaki & Mackinnon 1997).

To compare with a simple, unvarying state, we also calculate the energy distributions that result from a constant in time imposed electric field

$$\underline{E} = E_0 \hat{z} f(x, y) \tag{9}$$

where $f(x, y)$ is defined in Eq. (8). With its nonzero curl, this assumed form of E cannot represent a steady state reconnection. We employ it primarily to provide a simple, unvarying state for comparison with results in the time-dependent situation.

Key to understanding particle behaviour near the neutral point is the "adiabaticity" radius $r_{\rm ad}$, the distance from the neutral point at which the Larmor radius equals the magnetic field scale length. For $r > r_{\rm ad}$, particles move adiabatically. In other words, if the distance of the particle from the neutral point is of the order of its Larmor radius, then the particle is non-adiabatic.

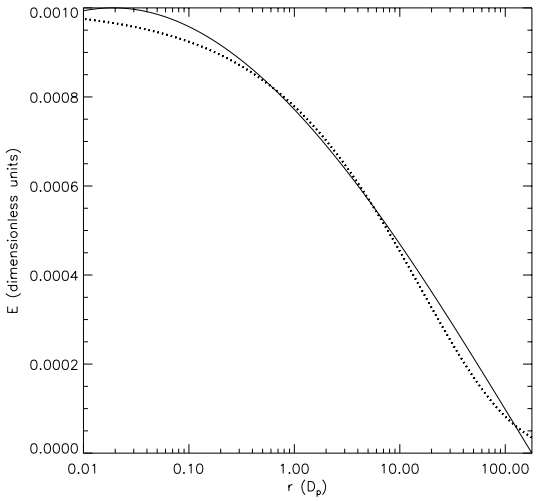

Fig. 1. Electric field (solid line) calculated from the Craig & McClymont (1991) solution for inertial resistivity $\eta = 3.1724 \times 10^{-11}$ and for the fundamental mode of azimuthal symmetry ($n = 0$) at $t = 0$. Approximate electric field described in Eq. (8) is shown in dotted line at $t = 0$.

The "adiabaticity" radius depends on the particle mass and velocity perpendicular to the magnetic field, $u_\perp$, and is given by

$$r_{\rm ad} = \left(\frac{mcDu_\perp}{eB_0}\right)^{\frac{1}{2}}. \tag{10}$$

For electrons and protons of the same energy, the electron gyroradius is $(\frac{m_{\rm e}}{m_{\rm p}})^{\frac{1}{2}}$ smaller than the proton gyroradius.

2.3. Numerical method

Due to the complexity of the orbits, their calculation cannot be done analytically. For integrating the ordinary differential equations (ODEs) describing the motion of the particles, we use the Bulirsch-Stoer method (Press et al. 1996). For a single particle with the same initial conditions, the orbit changes if the accuracy required of the integration routine is varied, and when the particle crosses the neutral point area (for general properties of X-type neutral point orbits see e.g. Martin 1986). The statistical properties of the *distribution* of test particles, which are of primary interest here, are unaffected by changes in the accuracy required of the integration routine. In the absence of an electric field, the routine conserves particle energy to one part in 10^{-5}.

We start the integration of particle orbits at $t = 0$ and with the particles positioned randomly in a box with the following size

$$-1.0 \leq x_0 \leq 1.0 \tag{11}$$

$$-1.0 \leq y_0 \leq 1.0 \tag{12}$$

$$z_0 = 0.0 \tag{13}$$

in electron or proton units depending on the species. We integrate the particle orbits up to 230 400 timesteps ($\tau_{\rm e}$) for electrons and 5360 timesteps ($\tau_{\rm p}$) for protons. With $B_0/D = 10^{-7}$ and our form of dimensionless units these times correspond to 1 s for electrons and protons. The initial velocities of the particles are picked randomly from a Maxwellian distribution of temperature 5×10^6 K (~431 eV), a typical coronal value. We consider only small values for $\bar{E}_0$, consistent with the passage of a disturbance in the linear regime (Craig & McClymont 1991). Values of 0.0001, 0.001 and 0.01 are used in the actual calculation.

The value 0.001 corresponds to electric field = 5.88×10^{-4} statvolt/cm. These are moderate values for electric fields present in the solar atmosphere (see Foukal et al. 1986).

2.4. Particle orbits

We are going to examine a typical proton orbit which is shown in Fig. 2. The amplitude of the time-varying electric field is $\bar{E}_0 = 0.001$ and the frequency is $\omega = 0.2$. In Fig. 2a we plot the (dimensionless) energy of the proton as a function of time for the interval $2400-5360\,\tau_p$. In Fig. 2b is shown the projection of the same orbit on the $X-Y$ plane and in Fig. 2c the projection of the same orbit on the $X-Z$ plane. Our model assumes a system scale of $\sim 178 D_p$, corresponding to a typical active region scale of 10^9 cm. In Fig. 2b we zoom in close to the neutral point to observe the particle orbit in detail and we look in an area of $-1.0D_p < \bar{x} < 1.0D_p$ and $-1.0D_p < \bar{y} < 1.0D_p$. In the same figure superposed in dotted line are some of the magnetic field lines showing the structure of the X-type magnetic neutral point. All field lines tend to the separatrices (shown in dashed lines) as the distance from the neutral point becomes very large.

The thick solid circle has radius $d = 10 r_{ad}$ for a thermal proton. Inside this region the gyroradius (Larmor radius) of most particles is not well defined since the particle is not bound to one magnetic field line and meandering motion is observed. The electric field accelerates or decelerates the proton causing further changes in the particle gyroradius and energy. This behavior resembles a stochastic-type acceleration. Stochasticity is introduced by the phase of the electric field and the phase of the particle orbit and is sustained because of the form of the magnetic field (e.g. Martin 1986). Outside the magnetic neutral point area the particle is moving along a particular magnetic field line. The gyroradius and the parallel velocity decrease as the particle moves away from the neutral point. The particle mirrors and recrosses the non-adiabatic region and the process is repeated until the end of the integration time or until the particle escapes the outer boundary of the system ($x, y \geq 178 D_p$).

Looking back at Fig. 2a we see the variation of the particle energy as a function of time. The intervals of energy conservation correspond to the times the particle is away from the nonadiabatic region, and in regions where the electric field is decreasing. Changes in the particle energy take place during the crossing of the non-adiabatic region.

The orbits of electrons show similar properties to those of the protons. Additionally from the way we pick our initial conditions the electrons start closer to the neutral point (see Sect. 2.2). But since the form of the electric field for both species is calculated assuming proton inertial resistivity, electrons see an area much larger than their adiabaticity radius where the electric field is close to its maximum value. Consequently some of the electrons start their motion outside their adiabaticity radius and their motion is immediately adiabatic. In this case the presence of the electric field does not increase their energy except if they eventually cross the non-adiabatic region.

The amount of acceleration that particles get depends on the time they spend close to the neutral point, on the phase of the orbit and on the frequency of the electric field. We define crossing time as the time the particle needs to cross the non-adiabatic region (Sect. 2.2) and is given to order of magnitude by

$$t_{cr} \sim \frac{2 r_{ad}}{u_{x,y}} \tag{14}$$

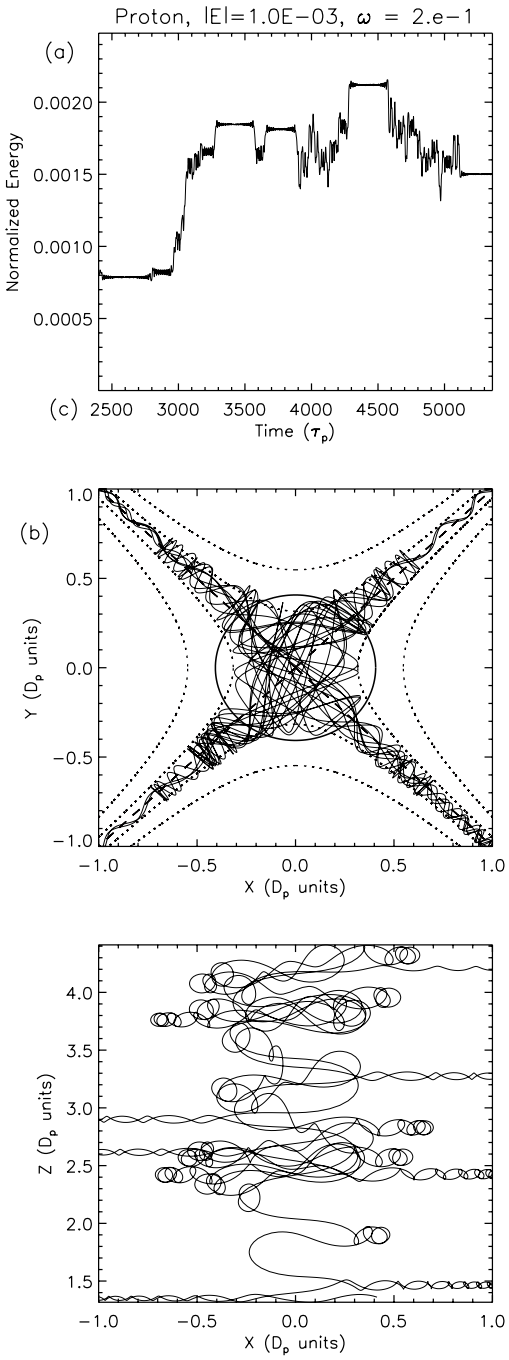

Fig. 2. Proton orbit in time-varying electric field of $\omega = 0.2$. **a)** Energy as a function of time **b)** Projection in the $X-Y$ plane. **c)** Projection in the $X-Z$ plane.

where $u_{x,y}$ is the velocity projection in the $x-y$ plane. So,

$$t_{cr} \sim \left(\frac{2.828 cD}{eB_0}\right)^{1/2} \frac{m_i^{3/4}}{E^{1/4}}. \tag{15}$$

It turns out that particles with the same energy satisfy

$$t_{cr_p} = t_{cr_e} \left(\frac{m_e}{m_p}\right)^{\frac{3}{4}} = 280 t_{cr_e} \tag{16}$$

where t_{cr_p} is the proton crossing time and t_{cr_e} is the electron crossing time. One would expect that in order to get particles

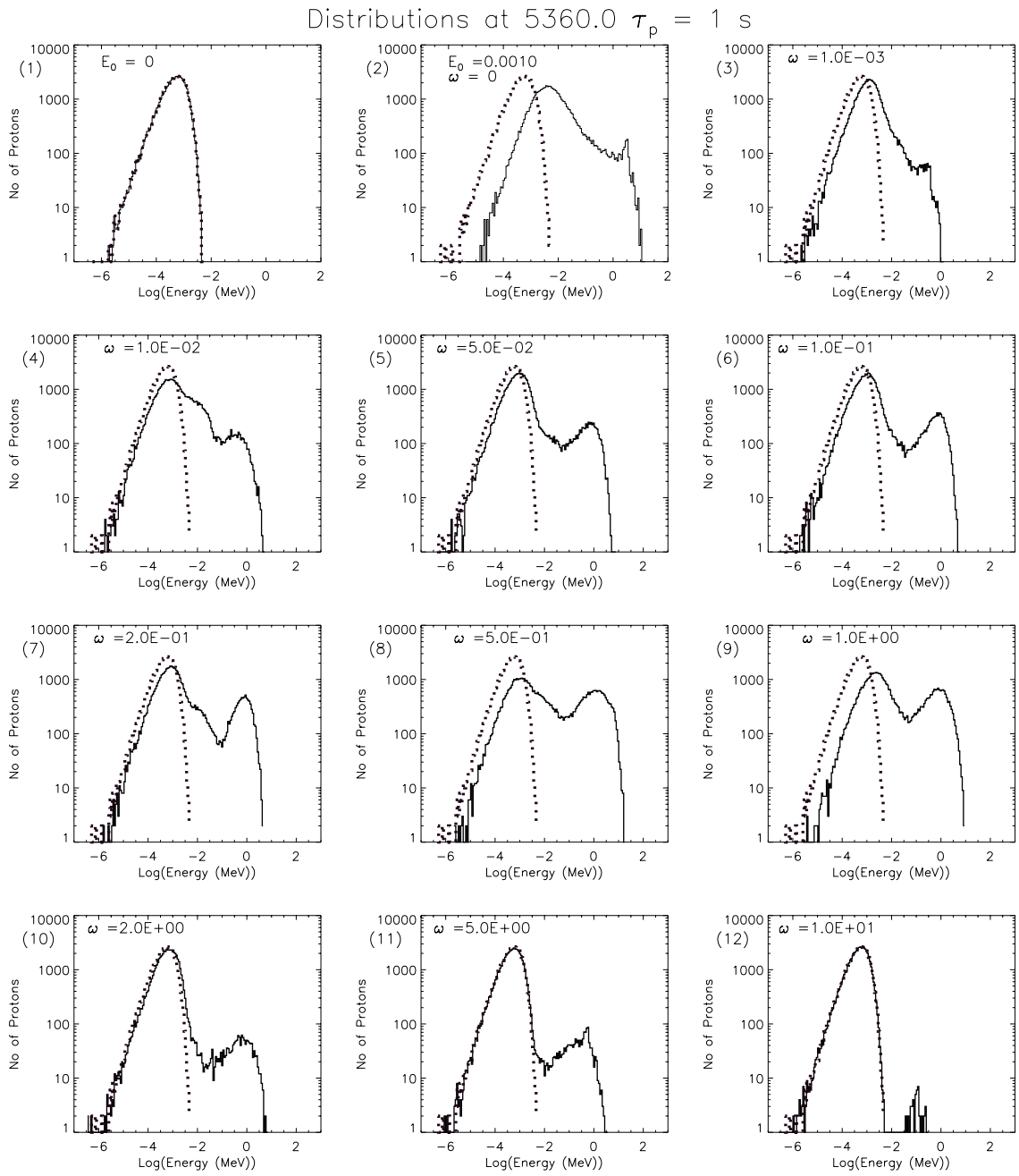

Fig. 3. Proton distributions for different frequencies of the electric field. The magnitude of the electric field is $\bar{E}_0 = 0.001$. The total integration time is 5360.

effectively accelerated (or decelerated since the sign of the electric field is not constant) we need $t_E \gg t_{\rm cr}$ where $t_E = 1/\omega$ is the period of fluctuation of the electric field. Thus we see potential for differences between electron and ion acceleration.

3. Energy distributions of accelerated electrons and protons

We calculate the kinetic energy of each particle up to maximum of a 1 s real time along with final positions and velocities. Particles in our calculation spend a relatively short time close to the neutral point but they get trapped in the magnetic configuration and re-cross the neutral point a number of times (Sect. 2.4). Particles encounter the non-adiabatic region, the process resulting in a Fermi-type acceleration. A similar phenomenon has been noted for a multiple neutral point configuration by Kliem (1994), in the behavior of protons in the presence of an MHD disturbance by Petkaki & Mackinnon (1997), and was explored analytically for time-varying electric field by Litvinenko (2003).

We sample the electric field frequency range $0.001 < \omega < 100$ for protons and $0.005 < \omega < 1000$ for electrons. In Fig. 3 we plot histograms of the logarithm of the initial and final energy distributions of protons, for magnitude of the electric field $\bar{E}_0 = 0.001$ and total number of timesteps 5360. Each distribution is generated using 50 000 test protons. We also calculated the distributions resulting when the magnitude of the electric field is $\bar{E}_0 = 0.01$ and $\bar{E}_0 = 0.0001$. The initial Maxwellian distribution is shown in dotted lines in each panel. Panel (1) shows the distributions for electric field magnitude $\bar{E}_0 = 0$. We observe no change in the form of the distribution since no

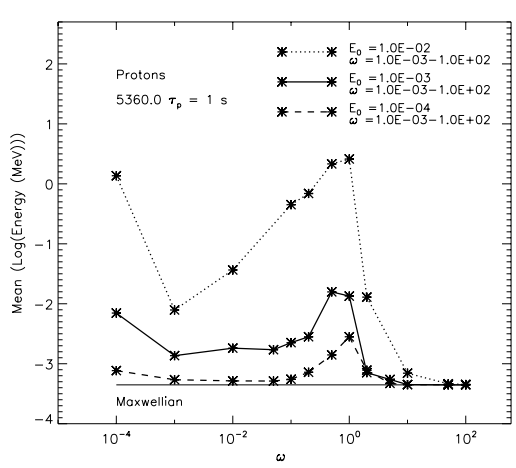

Fig. 4. Mean energy of proton distributions for three amplitudes of the electric field ($\bar{E}_0 = 0.0001, 0.001, 0.01$) and for range of frequencies 0.001 to 100.0. The mean energy of the initial Maxwellian distribution is shown as a straight full line. The constant electric field case is represented by $\omega = 0.0001$.

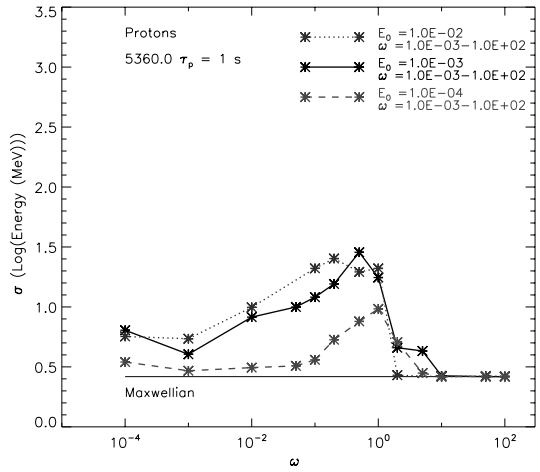

Fig. 5. Standard deviation of proton distributions for three amplitudes of the electric field ($\bar{E}_0 = 0.01, 0.001, 0.0001$) and for range of frequencies 0.001 to 100.0. The standard deviation of the initial Maxwellian distribution is shown as a straight full line. The constant electric field case is represented by $\omega = 0.0001$.

acceleration is taking place (see also Sect. 2.3). Panel (2) shows the energy distributions for constant electric field ($\omega = 0$) to provide a comparison with steady state magnetic reconnection. The final energy distribution for $\omega = 0$ has two distinct peaks, one at the initial Maxwellian distribution and a beamlike distribution close to $K_{\rm kin} = 10$ MeV. The energy distributions for constant electric field are not power laws as found elsewhere (see e.g. Bulanov & Sasarov 1976; Bruhwiler & Zweibel 1992). In those former calculations the particles crossed the neutral point only once, whereas particles recross the neutral point numerous times in our model. The frequency of the time-varying electric field increases progressively from $\omega = 0.001$ in panel (3) to $\omega = 10$ in panel (12). For $\omega = 0.001$ a small beamlike structure appears at $K_{\rm kin} = 0.3$ MeV. The final energy distributions are bi-modal from $\omega = 0.01$ to $\omega = 10$. For higher frequencies the proton energy distributions do not show significant energy changes.

In Fig. 4 we plot the mean of the logarithm of the initial and final proton energy distributions versus the frequency of the electric field and for three amplitudes of the electric field $\bar{E}_0 = 0.0001$ (dashed star line), $\bar{E}_0 = 0.001$ (solid star line), and $\bar{E}_0 = 0.01$ (dotted star line). The mean energy for the constant electric field is represented on this plot by $\omega = 10^{-4}$. The same representation is used in Fig. 5 where we plot the standard deviation of the logarithm of the initial and final proton energy distributions versus ω for the same three amplitudes of the electric field as in Fig. 4. We use the mean value of the logarithm of the energy to better represent the changes in highly non-thermal distributions.

The mean energy increases monotonically with $\bar{E}_0$ for the constant electric field case and for all frequencies of the electric field except for the highest frequency used in our model. The highest mean energy is achieved for constant electric field for all values of the electric field. For $\bar{E}_0 = 0.0001$ the highest energy gain for the time-varying electric field is achieved when $0.2 < \omega < 2.0$, indicating a resonant acceleration process. For $\bar{E}_0 = 0.001$ a peak in the mean energy is also present when $0.2 < \omega < 2.0$. For $\bar{E}_0 = 0.001$ protons gain most energy from the low ω electric field (see Fig. 4). When $\bar{E}_0 = 0.01$ protons a peak in the mean energy is present when $0.01 < \omega < 2.0$. For frequency $\omega = 10$ and greater the energy distribution does not change significantly for all values of $\bar{E}_0$.

In Fig. 6 we plot histograms of the logarithm of the initial and final energy distributions of electrons, for magnitude of the electric field $\bar{E}_0 = 0.001$ and total number of timesteps 230 480. Again we generate each distribution using 50 000 test electrons, and show the initial Maxwellian distribution in dotted lines in each panel. Panel (1) shows the energy distributions for non-varying electric field ($\omega = 0$). The final energy distribution (shown in solid line) includes a small beamlike component. The lower energy part of the final distribution is Maxwellian-like peaking at kinetic energy $K_{\rm kin} = 10^{-1}$ MeV, with a small beamlike component superposed at around kinetic energy $K_{\rm kin} = 1$ MeV. The frequency of the time-varying electric field increases progressively from $\omega = 0.001$ (panel 2) to $\omega = 500$ (panel 12). The bulk of the distribution is accelerated for the frequency range $\omega = 0.001$ to $\omega = 50$. Accelerated distribution for $\omega = 0.001$ (panel 2) is Maxwellian-like peaking around $\sim K_{\rm kin} = 10^{-2}$ MeV. From $\omega = 0.01$ (panel 3) to $\omega = 1$ (panel 6) the accelerated distributions have maximum close to $\sim K_{\rm kin} = 0.01$ MeV with maximum energy close to 1 MeV. From $\omega = 5$ (panel 7) to $\omega = 20$ (panel 9) the accelerated distributions have maximum close to $\sim K_{\rm kin} = 0.1$ MeV with maximum energy exceeding to 1 MeV. The final energy distributions are bi-modal for $\omega = 50$ to $\omega = 500$ containing a Maxwellian-like part at the energy range of the initial Maxwellian distribution and an accelerated part at higher energies with peak in the range $\sim K_{\rm kin} = 0.03$ to $\sim K_{\rm kin} = 0.7$ MeV. For higher frequencies the energy distributions do not show significant energy changes in the time of maximum 1 s.

The electron distribution gains energy for most of the frequencies of the electric field that we used in this model except for the highest frequencies. In Fig. 7 we plot the mean of the logarithm of the electron energy distributions versus ω for two amplitudes of the electric field $\bar{E}_0 = 0.0001$ (dashed star line), $\bar{E}_0 = 0.001$ (solid star line). In the same plot we superposed as error the standard deviation in the mean for each distribution. The mean energy for the constant electric field is represented on this plot by $\omega = 10^{-3}$. The highest energy gain achieved is for electric field with $\omega = 50$ for amplitude of the electric field $\bar{E}_0 = 0.001$. When $\bar{E}_0 = 0.0001$ electrons gain most energy for the constant electric field and for $\omega = 50$.

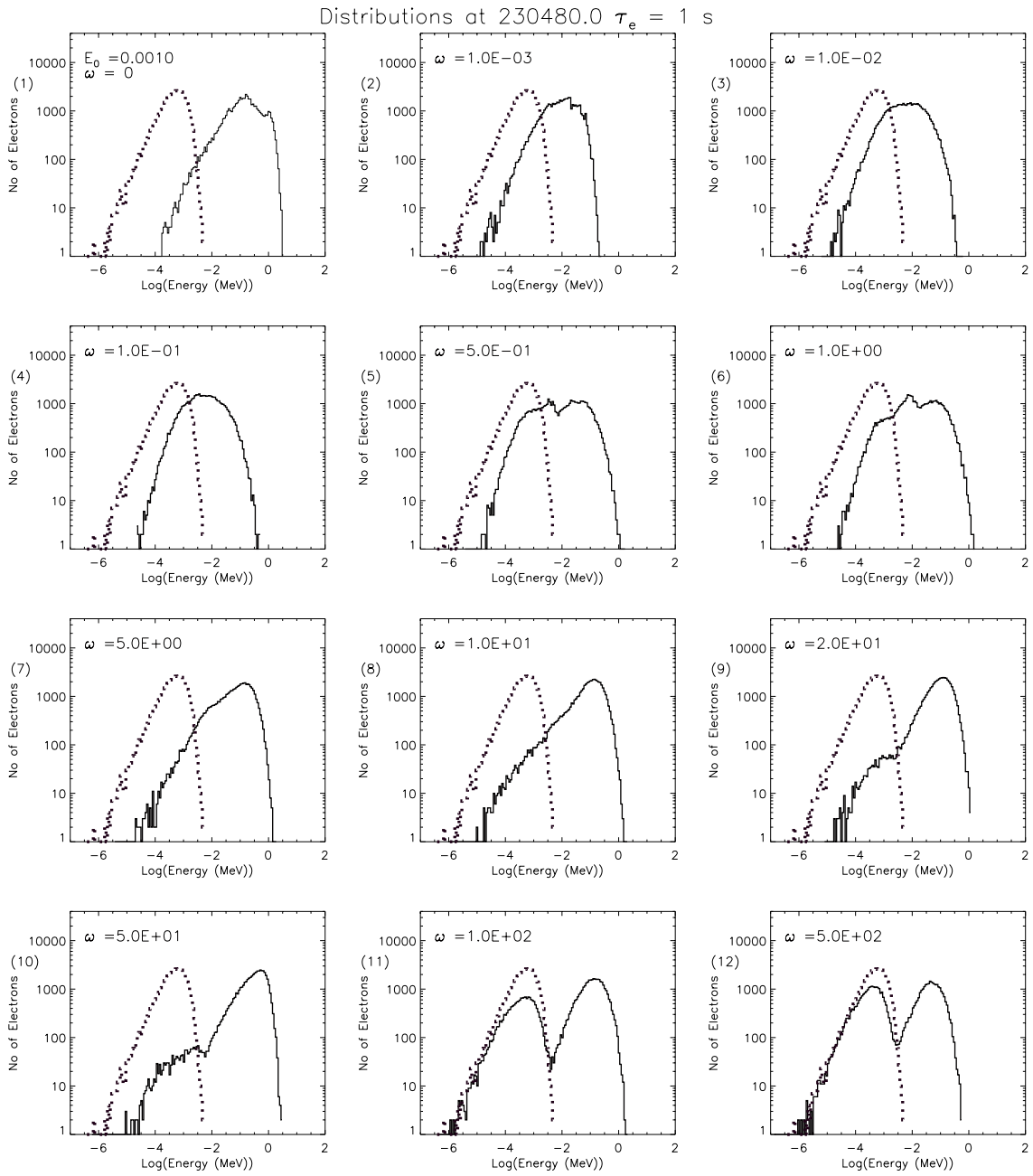

Fig. 6. Electron distributions for different frequencies of the electric field. The initial Maxwellian distribution is shown in dotted line on each panel. The magnitude of the electric field is $\bar{E}_0 = 0.001$. The maximum integration time of each particle trajectory is 230 480.

In the tables that follow we summarized the energy gain aspects of the acceleration mechanism. For each particle we find the energy gain using its initial and final kinetic energy, that is:

$$\frac{\Delta K^i}{K^i_{\rm initial}} = \frac{K^i_{\rm final} - K^i_{\rm initial}}{K^i_{\rm initial}} \tag{17}$$

where $K^i_{\rm initial}$ is the initial energy of the ith particle and $K^i_{\rm final}$ is the final energy of the ith particle. $\Delta K^i/K^i_{\rm initial} = A$, where A takes the values 1, 10, 100.

In Table 1 we list the accelerated percentage of the final proton distribution for each electric field frequency and for $E_0 = 0.001$. The first column lists the frequencies of the electric field. The second, third and fourth columns list the percentage of the final proton distribution for which A is greater than 1, 10 and 100 respectively (Eq. (17)). The fifth column lists the percentage of the final proton distribution that has energy greater than 1 MeV and the last column list the highest energy in the final proton distribution in MeV. We see that depending on the frequency of the electric field, ∼0.2% to ∼17.9% of the proton distributions get accelerated to γ-ray producing energies in 1 s.

In Tables 2 and 3 we list the accelerated percentage of the final proton distribution for each available electric field frequency for $E_0 = 0.0001$ and for $E_0 = 0.01$. The layout of these tables is the same as for Table 1 discussed before.

In Tables 4 and 5 we list the accelerated percentage of the final electron distribution for each available electric field frequency for $E_0 = 0.001$ and for $E_0 = 0.0001$ respectively. The first, second, third and fourth columns are layed out as in Table 1. The fifth column lists the percentage of the final electron

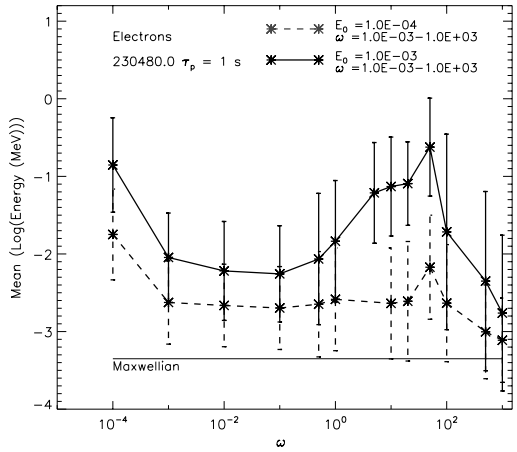

Fig. 7. Mean energy and standard deviation of electron distributions for two amplitudes of the electric field ($\bar{E}_0 = 0.001, 0.0001$) and for range of frequencies. The mean energy of the initial Maxwellian distribution is shown as a straight full line. The constant electric field case is represented in $\omega = 0.001$.

Table 1. Percentage of accelerated protons for $E_0 = 0.001$.

ω	>1	>10	>100	>1 MeV	(MeV)
0.0	89.1%	50.7%	14.5%	3.0%	15.9
0.001	59.7%	12.5%	2.9%	0.01%	1.31
0.01	47.9%	24.3%	8.8%	0.9%	5.86
0.05	51.0%	19.0%	11.1%	2.9%	8.0
0.1	55.2%	22.9%	14.3%	3.9%	5.9
0.2	52.9%	27.7%	17.8%	5.2%	5.0
0.5	72.7%	52.0%	37.4%	17.9%	18.5
1.0	82.3%	51.4%	32.6%	11.1%	9.33
2.0	30.9%	4.2%	2.4%	0.8%	7.33
5.0	6.0%	3.3%	2.3%	0.2%	3.8
10.0	0.3%	0.1%	0.01%	0.0%	0.31
50.0	0.0%	0.0%	0.0%	0.0%	0.005
100.0	0.0%	0.0%	0.0%	0.0%	0.005

Table 2. Percentage of accelerated protons for $E_0 = 0.0001$.

ω	>1	>10	>100	(MeV)
0.0	26.1%	4.0%	1.0%	0.36
0.001	9.6%	1.6%	0.2%	0.12
0.01	6.1%	2.3%	0.4%	0.13
0.05	0.14%	2.9%	0.7%	0.14
0.1	6.8%	4.3%	1.4%	0.17
0.2	12.6%	9.5%	4.6%	0.5
0.5	33.8%	24.0%	8.0%	0.96
1.0	51.1%	38.1%	15.0%	1.32
2.0	17.2%	11.5%	3.5%	0.21
5.0	2.9%	0.2%	0.0%	0.04
10.0	0.01%	0.0%	0.0%	0.012
50.0	0.0%	0.0%	0.0%	0.005
100.0	0.0%	0.0%	0.0%	0.005

distribution with energy greater than 20 keV and the last column lists the highest energy in the final electron distribution in MeV. For $E_0 = 0.001$ and for most frequencies of the electric field (and for constant electric field) the bulk of the electron distributions get accelerated to X-ray producing energies in the timescale of our model. When $E_0 = 0.0001$ only small percentage of the electron distribution accelerates to X-ray producing energies except for constant electric field where ∼50% accelerates to X-ray producing energies and

Table 3. Percentage of accelerated protons for $E_0 = 0.01$.

ω	>1	>10	>100	>1 MeV	(MeV)
0.0	100%	100%	99.2%	45.3%	525
0.001	92.9%	57.1%	12.8%	2.6%	24.5
0.01	98.4%	80.1%	38.9%	9.5%	237
0.1	99.8%	97.4%	67.8%	38.8%	225
0.2	99.8%	96.6%	69.3%	47.2%	197
0.5	99.8%	97.9%	84.9%	59.8%	202
1.0	99.6%	97.9%	88.5%	57.6%	343
2.0	97.1%	78.0%	15.6%	0.1%	56.5
10.0	40.6%	1.9%	0.04%	0.0%	0.18
50.0	3.0%	0.03%	0.0%	0.0%	0.005
100.0	0.4%	0.0%	0.0%	0.0%	0.005

Table 4. Percentage of accelerated electrons for $E_0 = 0.001$.

ω	>1	>10	>100	>20 keV	(MeV)
0	99.6%	97.0%	78.9%	91.6%	3.7
0.001	96.7%	71.9%	4.8%	29%	0.3
0.01	87.8%	59.5.6%	6.8%	22.8%	0.6
0.1	92.7%	50.4%	10.8%	20.9%	0.7
0.5	80.4%	60.4%	22.8%	39.6%	1.8
1.0	89.3%	72.2%	29.5%	44.5%	1.3
5.0	99.1%	92.8%	59.3%	78.6%	2.1
10.0	98.3%	93.2%	66.8%	85.0%	1.8
20.0	98.7%	95.8%	68.1%	89.6%	1.5
50.0	98.9%	97.2%	87.2%	94.9%	3.2
100.0	78.3%	68.4%	49.8%	65.3%	2.2
500.0	54.3%	50.6%	20.8%	43.9%	0.6
1000.0	41.3%	33.0%	3.9%	23.2%	0.3
10000.0	0.1%	0.00%	0.00%	0.00%	0.005

for $\omega = 50$ where ∼23% accelerates to X-ray producing energies.

Flare fast electrons as revealed by hard X-ray observations generally have energy distributions characterised by energy spectral indices in the range 2−5 (Dennis 1985). RHESSI data allow a less crude characterisation of the energy distribution (Kontar et al. 2005), but this range nonetheless gives a reasonable starting point for comparison with our results. With their high-energy peaks, sometimes bimodal in form, many of the distributions shown in Figs. 3 and 6 are clearly some way from those implied by observations. The electron distributions of Fig. 6 would give very hard photon spectra, harder than usually observed in flares. When segments of the distributions appeared to decline in energy in power-law form $E^{-\delta}$, we fit power-laws in energy to them, finding values of δ between about 1 and 2.5. Although we can account for particle acceleration in this way, to very high energies, we have to appeal to some other agent to redistribute energy among the accelerated particles to be compatible with observations. Very hard energy distributions are also found in most other calculations of acceleration in either one or many dissipation regions (e.g. Turkmani et al. 2006).

By fixing the duration of the integrations at 1 s we generate a snapshot of the distributions produced as particle acceleration proceeds. Obviously, particle energies will be less for shorter periods and greater for longer ones. As an illustration, in Fig. 8 we plot the time evolution of the logarithm of the mean energy of proton distributions for $\bar{E}_0 = 0.0001$, as functions of ω. Mean energy is plotted for 0.25 s (1340 τ_p), 1 s, and 2 s (10 720 τ_p). We observe that the greatest changes in mean proton energy take place for the lowest frequencies ω. At high frequencies, on the other hand, proton mean energy apparently changes little after 1 s. A sort of steady state is approached. Since no particles

Table 5. Percentage of accelerated electrons for $E_0 = 0.0001$.

ω	>1	>10	>100	>20 keV	(MeV)
0	98.7%	88.5%	0.0%	50.4%	0.43
0.001	75.5%	31.6%	0.0%	3.4%	0.07
0.01	76.4%	21.7%	0.6%	2.8%	0.12
0.1	72.5%	22.1%	1.9%	2.0%	0.097
0.5	60.6%	31.9%	4.3%	7.5%	0.18
1.0	65.5%	34.7%	5.0%	9.3%	0.13
10.0	63.0%	32.4%	4.0%	6.9%	0.1
20.0	61.9%	38.4%	4.7%	7.7%	0.082
50.0	84.6%	62.0%	11.2%	23.0%	0.28
100.0	60.2%	35.0%	3.6%	7.2%	0.11
500.0	39.5%	11.7%	0.5%	0.1%	0.036
1000.0	30.3%	6.7%	0.2%	0.0%	0.022

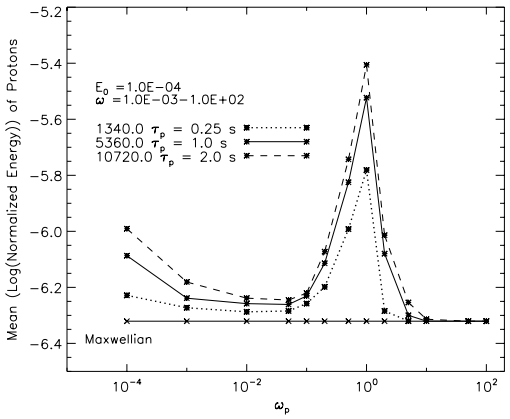

Fig. 8. Time evolution of logarithm of mean energy of protons for amplitude of the electric field ($\bar{E}_0 = 0.0001$) for constant electric field (represented on the graph by 0.0001) and for range of frequencies 0.001 to 100.0.

escape, this indicates a decrease with proton energy of the energy increment experienced on each return to the dissipation region: protons that can be accelerated at all no longer gain much energy after this time.

4. Discussion and conclusions

In this work we investigate the particle acceleration consequences of time-varying electric fields superposed on a X-type magnetic field to mimic generic features of dynamic, collisionless reconnection (Craig & McClymont 1991). We have shown that protons and electrons may gain relativistic energies in times ≤1 s; for plausible (small) electric field amplitudes and active region magnetic fields. This parametric study is meant to be complementary to Petkaki & MacKinnon (1997) where we attempted to tie this test-particle approach self-consistently to an MHD description of the passage of a wave. Although there are some qualitative similarities with the particle behaviour studied analytically by Litvinenko (2003), his adoption of a spatially uniform electric field makes direct comparison difficult.

Before discussing some consequences of our results, we note some limitations of our calculation. First, this is a test particle approach. Particles do not interact with each other, nor do they influence the background field. In particular, the particle distribution including the accelerated component may well be unstable to growth of various sorts of waves. Obviously such wave growth would influence the motion of particles, but we neglect this possibility. We neglect also radiation losses. In the solar corona this is not a serious neglect (even for 10 MeV electrons the radiative energy loss time is ∼3000 s), but elsewhere in the cosmos it could become significant.

We followed Craig & McClymont (1991) in assuming a smoothly varying X-type field through the whole of our system. We took the active region lengthscale of 10^9 cm to define the boundary of the system. It is possible that the field strength increases more rapidly from the neutral point, approaching a constant value at smaller distance. This would reduce both the adiabaticity radii of particles and the characteristic timescale. If we continued to scale the electric field region with the proton adiabaticity radius, nothing would change except that the integration periods correspond to smaller real times. Thus particle acceleration would proceed more rapidly; however, fewer particles would be involved. Further consideration of this question might proceed via study of more realistic configurations including a neutral point or sheet (e.g. Forbes & Priest 1995; Fletcher & Martens 1998; Titov & Démoulin 1999) or complex magnetic field structures (e.g. Malara et al. 2000).

The finite width of the nonadiabatic region allows particles to gain or lose some energy randomly before returning to adiabatic motion. Together with repeated encounters with the dissipation region, the consequence of mirrorings in the extended configuration, this results in a Fermi-type, "stochastic" acceleration.

In our model particle acceleration takes place for geometrical reasons. The test particle calculation is numerically simpler than self-consistent approaches (e.g. Vlasov simulations, see Petkaki et al. (2003, 2006) and gives useful insights to the particle energization process. There is no threshold for this type of acceleration, unlike resonant interaction with low-frequency, MHD waves. The necessity for protons particularly to have threshold energies of around 25 keV is a well known difficulty when such mechanisms are invoked (e.g. Forman et al. 1986). Our results indicate that low-frequency waves may themselves perform the "first-step" acceleration, if they propagate in a coronal structure including a neutral point. This may occur independently of, or simultaneously with, the resonant cascade scenario of Miller & Vinas (1993). Possible difficulties with the number of pre-accelerated particles may be obviated if many neutral points are present, although such a situation obviously needs separate investigation (Kliem 1994).

Most of the resulting proton distributions have a bi-modal form (see Fig. 3). Electron distributions are also bi-modal for the highest frequencies, $20 \leq \omega \leq 500$ (see Fig. 6). Whereas for the lowest frequencies of the electric field the bulk of the initial electron Maxwellian distribution is accelerated, for the highest frequencies only part of the electron distribution is accelerated (Table 4). Acceleration occurs for all frequencies $\omega \leq 10$ when addressing the proton distributions (Table 1). The bi-modal form of the proton energy distributions might offer a way to have protons of gamma-ray producing energies ($K_{\rm kin} \sim 2$ MeV) without the energetically dominant population at lower energies that is the inevitable consequence of a diffusive particle accelerator (see the Appendix of Eichler 1979; & MacKinnon 1991). Investigation of the velocity space stability of these distributions needs details of the angular distribution at particular points in space, and is not discussed here.

We note the effectiveness of acceleration of the two species varies according to the frequency of oscillation invoked. Electrons are accelerated for a broader spectrum of frequencies. Frequencies 0.001 to 1000 have been simulated here, corresponding to real frequencies in the range 5 Hz to 5 MHz (cf. the frequency range of waves from the base of the solar corona, probably in the range 0.01 Hz to 10 KHz, e.g.

Marsch et al. 1982). Frequencies lower than 0.001 will also accelerate electrons as indicated by the net acceleration achieved for the constant electric field cases (Fig. 7), but frequencies higher than 1000 do not produce a net acceleration in the timescale of our model.

Considered as a function of ω, the mean energy of the accelerated electron distribution exhibits a peak in the broad range $5 < \omega < 100$. Such a peak leads us to suspect a resonance involving two or more of the timescales in the problem. The initial gyrofrequencies of electrons lying in the adiabatic portion of the dissipation region also generally lie in this range. Inverse crossing times ($1/t_{\rm cr}$, see Eq. (14)) comparable with ω might also lead to enhanced acceleration. Using Eq. (14), but taking account also of the mean increase in $u_{x,y}$ we do indeed find upper limits in the range $5 < 1/t_{\rm cr} < 100$.

Protons are accelerated for low electric field frequencies, achieving γ-ray producing energies in 5360 $\tau_{\rm p} = 1$ s for frequencies $\omega < 10$ and for $E_0 = 0.001$ and $E_0 = 0.01$. A local peak in the mean energy of the accelerated proton distribution is seen at $0.1 < \omega < 2.0$. This range of frequencies are comparable to the gyrofrequencies of protons in the adiabatic region for our set of initial conditions and to the proton inverse crossing time.

The variability of the effectiveness of acceleration of the two species according to the frequency of electric field oscillation might bear on the apparent variation of electron/proton ratios in flares (Ramaty & Murphy 1987) and the phenomenon of "electron-only" flares (Rieger 1989). As a general comment, we note that higher frequency disturbances favour electrons over ions, although more definitive statements will need a proper treatment involving a more realistic wave.

For most frequencies and for constant electric field, part of the electron distribution escapes from the system boundaries before $230\,400\tau_{\rm e} = 1$ s. Electrons on average escape in less than 0.6 s in the frequency range $10 \leq \omega \leq 50$. Protons on the other hand do not escape the system boundaries on the same timescale of $5360\tau_{\rm p} = 1$ s for $E_0 = 0.001$ and $E_0 = 0.0001$. Electrons are accelerated more rapidly than protons to energies that do not allow them to mirror inside our system boundaries.

Here and in Petkaki & MacKinnon (1997) we investigate particle acceleration at a null in the presence of a linear disturbance. Such calculations may give some insight into particle acceleration in flares, although conditions then presumably depart severely from linearity, but might be most relevant to quiescent, long-lasting phenomena such as radio noise storms. Definitely involving deka-keV electrons (Raulin & Klein 1994) and showing correlations with X-ray variations, but without chromospheric, flare-like signatures (Svestka et al. 1986; Crosby et al. 1996), particle acceleration in noise storms might occur as described here, if the relevant coronal structures include null points. Electrons accelerated at a neutral point will likely encounter very large mirror ratios, trapping them in the corona (Fletcher & Martens 1998) and accounting for the exclusively coronal phenomena accompanying noise storms.

References

Aschwanden, M. J. 2002, Space Sci. Rev., 101, 1
Bruhwiler, D. L., & Zweibel, E. G. 1992, JGR, 97, 10825
Bulanov, S. V., & Sasarov, P. V. 1976, Soviet Astron., 19, 464
Burkhart, G. R., Drake, J. F., & Chen, J. 1990, JGR, 95, 18833
Burkhart, G. R., Drake, J. F., & Chen, J. 1991, JGR, 96, 11539
Craig, I. J. D., & McClymont, A. N. 1991, ApJ, 371, L41
Craig, I. J. D., & McClymont, A. N. 1993, ApJ, 405, 207
Crosby, N., Vilmer, N., Lund, N., Klein, K.-L., & Sunyaev, R. 1996, Sol. Phys., 167, 333
Dalla, S., & Browning, P. K. 2005, A&A, 436, 1103
Dennis, B. R. 1985, Sol. Phys., 100, 465
Efthymiopoulos, C., Gontikakis, C., & Anastasiadis, A. 2005, A&A, 443, 663
Eichler, D. 1979, ApJ, 229, 409
Fletcher, L., & Martens, P. 1998, ApJ, 505, 418
Forbes, T. G., & Priest, E. R. 1995, ApJ, 446, 377
Forman, M. A., Ramaty, R., & Zweibel, E. G. 1986, The acceleration and propagation of solar flare energetic particles, in Physics of the Sun, ed. P. A. Sturrock et al. (Kluwer), 2, 249
Foukal, P., Hoyt, C., & Gilliam, L. 1986, Apj, 303, 861
Gontikakis, C., Efthymiopoulos, C., & Anastasiadis, A. 2006, MNRAS, 368, 293
Greene, J. M. 1988, JGR, 93, 8583
Hamilton, B., McClements, K. G., Fletcher, L., et al. 2003, Sol. Phys., 214, 339
Hanasz, M., & Lesch, H. 2003, A&A, 404, 389
Heerikhuisen, J., Litvinenko, Y. E., & Craig, I. J. D. 2002, ApJ, 566, 512
Hudson, H. S. 1978, ApJ, 224, 235
Kliem, B. 1994, ApJS, 90, 719
Kontar, E. P., Emslie, A. G., Piana, M., Massone, A. M., & Brown, J. C. 2005, Sol. Phys., 226, 317
Kuijpers, J. 1993, Physics of Flares in Stars and Accretion Disks, in The Sun: A Laboratory for Astrophysics, ed. J. Schmeltz, & J. C. Brown (Kluwer), 535
Kuijpers, J., & van der Hulst, J. M. 1985, A&A, 149, 343
Litvinenko, Y. E. 2003, Sol. Phys., 216, 189
MacKinnon, A. L. 1991, Vistas Astron., 34, 331
MacKinnon, A. L. 2006, in Solar Eruptions and Energetic Particles, ed. N. Gopalswamy, R. Mewaldt, & J. Torsti, AGU
Malara, F., Petkaki, P., & Veltri, P. 2000, ApJ, 533, 523
Marsch, E. K., Goertz, C. K., & Richter, K. 1982, JGR, 87, 5030
Martens, P. C. H. 1988, ApJ, 330, L131
Martin, R. F. 1986, JGR, 91, 11985
McClements, K. G., Shah, N., & Thyagaraja, A. 2006, J. Plasma Phys., 72, 571
McClymont, A. N., & Craig, I. J. D. 1996, ApJ, 466, 487
Miller, J. A. 1998, Space Sci. Rev., 86, 79
Miller, J. A., & Vinas, A. F. 1993, ApJ, 412, 386
Øleroset, M., Phan, T. D., Fujimoto, M., Lin, R. P., & Lepping, R. P. 2001, Nature, 412, 414
Petkaki, P. 1996, Particle Acceleration in Dynamical Collisionless Reconnection, Ph.D. Thesis, University of Glasgow
Petkaki, P., & MacKinnon, A. L. 1994, Space Sci. Rev., 68, 117
Petkaki, P., & MacKinnon, A. L. 1997, Sol. Phys., 172, 279
Petkaki, P., Watt, C. E. J., Horne, R. B., & Freeman, M. P. 2003, JGR, 108, 1442
Petkaki, P., Freeman, M. P., Kirk, T., Watt, C. E. J., & Horne, R. B. 2006, JGR, 111, A01205
Press, W. H., Teukolsky, S. A., Vetterling, W. T., & Flannery, B. P. 1996, Numerical Recipes in FOTRTAN 90 (Cambridge: Cambridge University Press)
Priest, E. R., & Forbes, T. A. 2001, Magnetic Reconnection: MHD Theory and Applications (Cambridge: Cambridge University Press)
Ramaty, R., & Murphy, R. J. 1987, Space Sci. Rev., 45, 213
Rieger, E. 1989, Solar Phys., 121, 323
Raulin, J.-P., & Klein, K.-L. 1994, A&A, 281, 536
Senanayake, T., & Craig, I. J. D. 2006, A&A, 451, 1117
Smith, D. F. 1980, Sol. Phys., 66, 135
Speiser, T. W. 1970, Planet. Space Sci., 18, 613
Svestka, Z., Dennis, B. R., Pick, M., et al. 1982, Sol. Phys., 80, 143
Titov, V. S., & Démoulin, P. 1999, A&A, 351, 707
Tsuneta, S., et al. 1984, ApJ, 280, 887
Turkmani, R., Cargill, P. J., Galsgaard, K., Vlahos, L., & Isliker, H. 2006, A&A, 449, 749
Vainchtein, D. L., Buchner, J., Neishtadt, A. I., & Zelenyi, L. M. 2005, Nonlinear Processes in Geophysics, 12, 101
Wood, P., & Neukirch, T. 2005, Sol. Phys., 226, 73